Naphthalene diimides (NDI) in highly stable pH-neutral aqueous organic redox flow batteries

Journal of Electroanalytical Chemistry 896 (2021) 115224

Contents lists available at ScienceDirect

Journal of Electroanalytical Chemistry

journal homepage: www.elsevier.com/locate/jelechem

Naphthalene diimides (NDI) in highly stable pH-neutral aqueous organic redox flow batteries

Cedrik Wiberg [b], Lars Evenäs [b], Michael Busch [c], Elisabet Ahlberg [a,*]

[a] Department of Chemistry and Molecular Biology, Gothenburg University, 412 96 Gothenburg, Sweden
[b] Department of Chemistry and Chemical Engineering, Chalmers University of Technology, 412 96 Gothenburg, Sweden
[c] Department of Chemistry and Material Science, School of Chemical Engineering, Aalto University Kemistintie 1, 02150 Espoo, Finland

ARTICLE INFO

Keywords:
Energy efficiency
Capacity utilization
Electrochemistry
Self-association
DFT

ABSTRACT

In the pursuit of environmentally friendly energy storage, aqueous organic redox flow batteries (AORFBs) that use naphthalene diimide hold promise for successful application. In the present article, two different naphthalene diimides (NDI) are studied as negative electrolyte materials for pH-neutral aqueous organic/organometallic redox flow batteries. The two molecules, one core-unsubstituted NDI (2H-NDI) and one core-dimethylamino substituted NDI (2DMA-NDI) are coupled with a solubilized ferrocene (BTMAP-Fc) at a concentration of 50 mM in phosphate buffered potassium chloride. High energy efficiencies and coulombic efficiencies were obtained for both batteries, but a gradual capacity fade was observed while cycling. However, when changing the cation of the supporting electrolyte from potassium to ammonium, similar energy and coulombic efficiencies were obtained, but with undetectable capacity losses over 320 cycles. Finally, 2H-NDI and BTMAP-Fc at 500 mM were tested in the ammonium-based electrolyte, and while obtaining high coulombic efficiency, the energy efficiency and cycling stability decreased compared to the same system at lower concentration. It is concluded that loss of activity is mainly due to formation of electrochemically inactive compounds and that the electrolyte cation is of great importance for the outcome. Important design strategies for AORFB molecules include using supporting salts that prevent self-association and introducing sterically hindering substituents to the structures.

1. Introduction

Electricity generated by solar and wind has increased exponentially since the 1990s in order to minimize dependence on fossil fuels. However, due to the intermittency of the sources, electricity grid systems develop a growing dependency on energy storage as the portion of renewables increases.[1] A highly promising candidate for grid-connected energy storage is aqueous organic redox flow batteries (AORFBs) due to their low cost and ability to decouple power output and storage capacity.[2–8]

A seminal work in 2014 where 9,10-anthraquinone-2,7-disulfonic acid (AQDS) was coupled with bromide in a flow battery with promising performance[9] generated a large number of research groups pursuing high-performing organic molecules for this application.[10–18] Previous AORFB studies have often focused on the performance of quinones as redox-active material,[2,11,19–23] where the list of organic non-quinone materials is considerably shorter, and is largely limited to ferrocene,[16] TEMPO[14,15,24] and viologen.[16,25]

One type of molecule that has a similar redox behavior to quinones is 1,4,5,8-naphthalene diimide (NDI). It has a rich chemistry due to the possibility of modifying its electronic properties by chemical substitution on the naphthalene core,[26] while its solubility and self-associative properties can be tuned by choice of the side chain, which reaches from the imide nitrogen.[26] NDI has been thoroughly utilized in polymer solar cells on account of its high chemical stability and tunable electronic properties.[27,28] Due to its large planar aromatic core, the molecule is known to self-associate into different motifs depending on functionalization and molecular environment,[26,29–31] and has also proven to be suitable as a threading DNA intercalator.[32] In applications related to electrochemistry, NDI has been investigated as a sensor for organic molecules[33,34] and as cathode for lithium ion based batteries.[35–37]

We previously evaluated core-unsubstituted NDI with a propyldimethylamino sidechain, here called 2H-NDI, and found that the molecule's strong self-associative behavior has a significant effect on its aqueous electrochemistry on the cyclic voltammetry (CV)

* Corresponding author.
E-mail addresses: lars.evenas@chalmers.se (L. Evenäs), michael.busch@aalto.fi (M. Busch), elisabet.ahlberg@gu.se (E. Ahlberg).

https://doi.org/10.1016/j.jelechem.2021.115224
Received 25 January 2021; Accepted 28 March 2021
1572-6657/

timescale.[38] Galvanostatic cycling in a bulk electrolysis cell, however, showed that close to the theoretical capacity was accessed with little to no degradation of the molecule.[38] The effect of core-substitution on the electrochemistry of NDIs in aqueous solution has been investigated experimentally and computationally by our group and reductive pathways were presented for nine investigated species.[39] Five out of the nine NDI species were identified to be of particular interest to investigate experimentally for AORFB applications.[39]

Only two previous articles present the use of NDI in AORFBs. Firstly, an NDI molecule with a glycine sidechain was coupled with 4-OH-TEMPO in a flow battery that delivered good performance, albeit with a limited solubility of the NDI of 30 mM and 40 mM in 1 M KCl and NaCl electrolytes respectively.[40] Secondly, an NDI-polymer was demonstrated together with 2,7-AQDS in a redox flow battery that used a single mediator redox targeting reaction as mode of operation.[41] The battery showed a high degree of capacity retention, which further underlines the electrochemical stability of naphthalene diimides in aqueous solution.

In the present article, the operation of redox flow batteries with core–unsubstituted, N,N'-bis(dimethylaminopropyl)-NDI (short 2H-NDI) or N,N'-bis(dimethylaminopropyl)-2,6-bis(dimethylamino)-NDI (short 2DMA-NDI), is investigated. A total of five different neutral aqueous redox flow batteries using 2H-NDI or 2DMA-NDI coupled with 1,1′-Bis[3-(*trimethylammonio*)*propyl*]ferrocene dichloride (BTMAP-Fc) are studied with respect to the effect of self-association, electrolyte cation and concentration on battery performance.

BTMAP-Fc is a water-solubilized ferrocene that was coupled with a modified viologen molecule in a system that reported a per-cycle capacity retention exceeding 99.99% at high concentrations.[16] The stability, solubility and commercial availability of BTMAP-Fc makes it a good model compound to test negative electrolytes against.

The voltages of the batteries, which are shown in Table 1, are relatively low compared to many other reported systems.[2,42] However, as the scope of this article is to evaluate the performance of 2H-NDI and 2DMA-NDI in negative electrolytes, the commercial availability and proven cycling stability of BTMAP-Fc was considered more important than demonstrating a battery with a high voltage.[16] It is identified that if a TEMPO-based species had been used instead of BTMAP-Fc, a 0.41 V higher voltage would have been achieved throughout.[2,12,40]

2. Results and discussion

A summary of the studied redox flow batteries is shown in Table 1.

After the assembly of a battery, the ohmic resistance was determined using impedance spectroscopy at the open circuit voltage. After this, the battery was charged and discharged for three cycles at a set of current densities ranging between 5 and 60 mA cm^{-2} to obtain information on its rate performance. Lastly, a larger amount of charging and discharging cycles was carried out at a given current density to investigate the stability of the system. While the NDIs are reduced with two electrons,[38] BTMAP-Fc is only oxidized with one,[43] and therefore, to keep the capacities of the electrolytes balanced, their volumes were 10 ml and 20 ml respectively. The pH of the electrolytes was adjusted to 7 and preserved by the phosphate buffer. The voltage cut-offs for the first 142 cycles of RFB-1 were set to −0.3 V and 1.3 V but were narrowed to 0 V and 1.2 V for all the following experiments, if not stated otherwise. In the cycling experiments, charging (reducing NDI) is shown as increasing cell potentials with increasing charge and vice versa for discharging.

CVs of 2H-NDI, 2DMA-NDI and BTMAP-Fc are shown in Fig. 1a. At neutral pH, 2H-NDI has two redox couples, the first at −0.28 V, corresponding to 2H–NDI + $e^- \rightleftharpoons$ 2H-$NDI^{\bullet}$, and this is referred to as the *first redox couple* in the following discussion, regardless of whether occurring during charge or discharge. The second occurs at −0.62 V and corresponds to 2H–$NDI^{\bullet}$ + $e^- \rightleftharpoons$ 2H-NDI^{2-},[38] and is consequently referred to as the *second redox couple*. Apart from these two, a small current corresponding to an additional redox couple is seen at a potential about 100 mV in the negative direction of the first redox couple and is thought to be the result of self-association.[38] As the self-association most likely only involves 2H–NDI and/or 2H-$NDI^{\bullet}$, to simplify the following discussion, the capacity of the shoulder is counted as belonging to the *first redox couple*.

The CV of 2H-NDI in Fig. 1a was referenced against BTMAP-Fc and laid over the charging/discharging curves from the first cycle of RFB-1, see Fig. 1b. It is seen that the two redox couples give rise to two voltage plateaus during cycling, and that a shoulder appears at 0.6 V on the charging curve that matches the peak that was attributed to the self-association of 2H-NDI.

2.1. 2H-NDI vs BTMAP-Fc

2.1.1. 50 mM 2H-NDI/BTMAP-Fc in 1 M KCl and 0.5 M KPhos

As a first redox flow battery test, 2H-NDI was coupled with BTMAP-Fc at a concentration of 50 mM in 0.5 M potassium phosphate (KPhos) buffer at pH 7, which also contained 1 M potassium chloride for increased conductivity, see Fig. 2. The cell, here called RFB-1, was cycled at 10 mA cm^{-2} for 142 cycles with voltage cut-offs at −0.3 V and 1.3 V. The battery had a good coulombic efficiency of 99.72(2)% and an energy efficiency of 87% at 10 mA cm^{-2}, see Fig. 2e. However, Fig. 2c shows that the capacity of the first redox couple decreased quite rapidly during cycling compared to the capacity of the second redox couple. A similar phenomenon was recently reported when cycling an NDI with glycine–based sidechains and was attributed to the trapping of potassium ions between the imide oxygen atoms and the glycine group.[40] If the same phenomenon occurs in the present work, the potassium trapping would be limited to the imide oxygens due to the positively charged sidechains

To quantify this behavior, the point on each charging and discharging curve with the highest value of dE/dQ was identified for each cycle (excluding the areas close to the voltage cut-offs), where E and Q is the voltage and capacity respectively. The capacity at this point was established as corresponding to the first redox couple during charge, and the remaining capacity was counted to the capacity of the second redox couple during charge. Fig. 2d was constructed from this data and shows an interesting cycling behavior. During charging, the

Table 1
Summary of the investigated redox flow battery (RFB) chemistries.

#	Conc.	Active material	Background electrolyte	Voltage[a]	Ohmic resistance	Cycling time
RFB-1	50 mM	2H-NDI / Fc[b]	1 M KCl + 0.5 M KPhos[c]	0.65 V	0.63 Ohm	192 h
RFB-2	50 mM	2H-NDI / Fc	1 M NH_4Cl + 0.5 M NH_4Phos	0.67 V	1.07 Ohm	156 h
RFB-3	500 mM	2H-NDI / Fc	1 M NH_4Cl + 0.5 M NH_4Phos	0.65 V	0.66 Ohm	212 h
RFB-4	50 mM	2DMA-NDI / Fc	1 M KCl + 0.5 M KPhos	0.62 V	0.57 Ohm	88 h
RFB-5	50 mM	2DMA-NDI / Fc	1 M NH_4Cl + 0.5 M NH_4Phos	0.65 V	0.67 Ohm	173 h

[a] *Calculated from the average charging and discharging voltages.*
[b] *Fc = BTMAP-Fc,* [c] *Phos = Phosphate.*

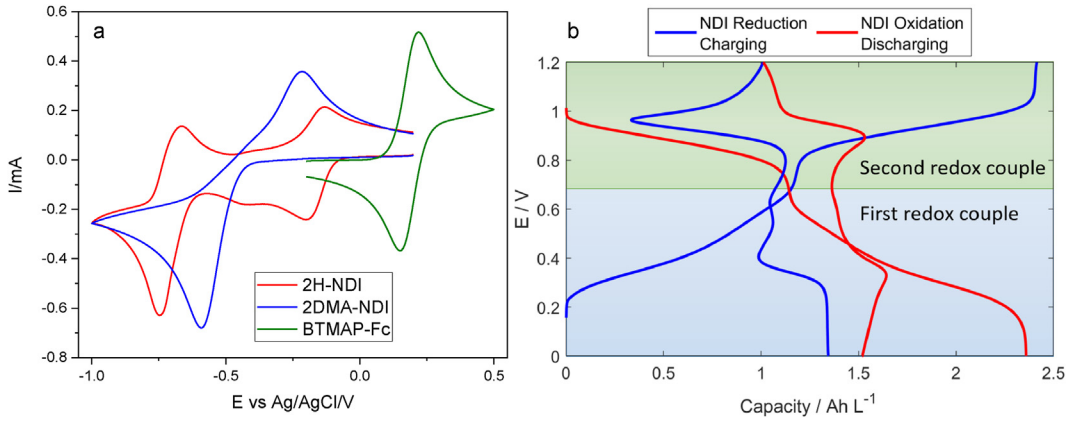

Fig. 1. a) CVs of 50 mM 2H-NDI, 2DMA-NDI and BTMAP-Fc in 1 M KCl and 0.5 M KPhos. Sweep rate: 100 mV s^{-1}. b) Charging/discharging curves of RFB-1 overlaid with the CV of 2H-NDI. Current density: 5 mA cm^{-2}.

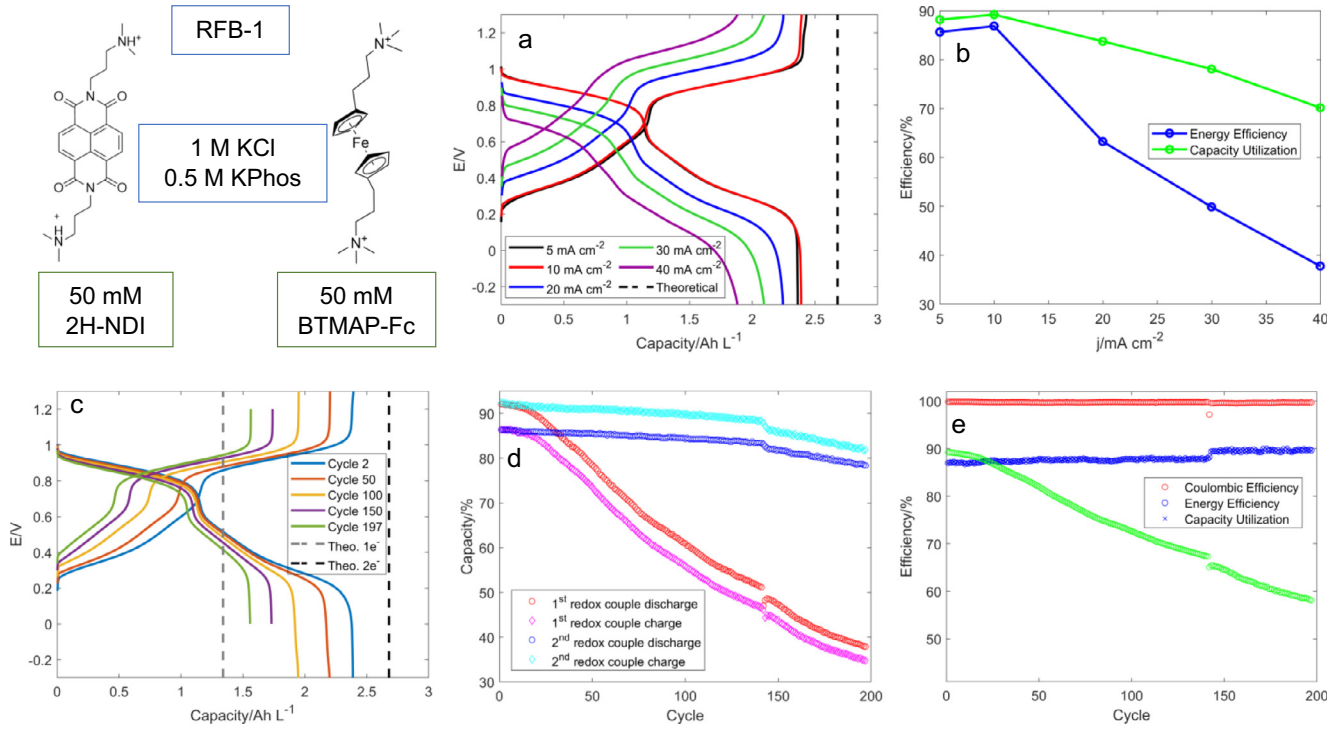

Fig. 2. Flow battery performance of 50 mM 2H-NDI/BTMAP-Fc in 1 M KCl and 0.5 M KPhos. a) Charging and discharging curves at varying current densities, b) energy efficiency and capacity utilization at varying current densities c) charging and discharging curves at selected cycles, d) charge and discharge capacity utilization for the first and second redox couples and e) efficiencies. For the long-term cycling, a current density of 10 mA cm^{-2} was used for the first 142 cycles, and then decreased to 5 mA cm^{-2} for the remaining cycles.

plateau for the first redox couple reaches a slightly lower capacity than for the second, but for discharging, the trend is reversed. The reason for this behavior is treated in Section 2.3.

After 142 cycles, the current density was decreased to 5 mA cm^{-2} and the voltage cut-offs narrowed to 0 V and 1.2 V for 54 cycles, to see if this would diminish the capacity decrease. The capacity fade, however, continued unabated, see Fig. 2d and e. The coulombic efficiency at 5 mA cm^{-2} was 99.63(5)%. CVs after the total of almost 200 cycles were recorded on each electrolyte, see Figure S1a. The reduction current for 2H-NDI after cycling was significantly lower than before cycling, which shows that 2H-NDI has reacted and formed electrochemically inactive compounds. This also explains the decrease in capacity utilization seen in Fig. 2e. 2H-NDI is known to self-associate and prolonged cycling seems to build up larger aggregates with limited redox activity.[38,40] No visible amounts of 2H-NDI had crossed over to the ferrocene side, likely due to the larger size of the self-associated complexes than of the monomers. A small amount of cross-over of Fc was observed.

2.1.2. Further cycling experiments of RFB-1

Before disassembling RFB-1, the voltage was held at −0.5 V for two hours to see if this would recover some of the lost capacity due to self-association. However, no effect on the capacity was seen, see Figure S10.

The electrolytes, electrodes and the membrane of RFB-1 was replaced three times to generate three new batteries, in order to study the impact of temperature and cycling strategies on the

self-association. The data related to these batteries are presented in SI sections 5 – 7.

The second iteration of RFB-1, RFB-1.1, was studied at an increased temperature of 40 °C. It was envisioned that the increased temperature might have an effect on self-association. Summarily, the capacity decreased more rapidly than at room temperature. Once the capacity had decreased to 27% of its theoretical value, the battery was disassembled, and a CV was recorded on each electrolyte. In addition to a general decrease of the current after cycling, an oxidation peak on the 2H-NDI side at −0.03 V vs Ag/AgCl had appeared and was attributed to a degradation or complexation product of 2H-NDI, see Figure S14. The cross-over of Fc is also larger compared with the experiment at room temperature, which contributes to the decrease in capacity.

In the third iteration, RFB-1.2, discharge potential cut-offs of −0.3 V and −0.5 V were tested, but no effect on the efficiencies or capacities was seen. The potential cut-off while charging was kept at 1.2 V. After 120 cycles, the cycling was stopped for 100 h while the pump was left on. After beginning cycling again, the capacity corresponding to the first redox couple had dropped by approximately 20% but recovered slightly on the following cycles, Figure S15.

In a last iteration, RFB-1.3, every 10th charging step was followed by a potentiostatic hold at 1.2 V. This was done to study whether the self-association equilibria could be driven toward higher redox activity by consuming all the 2H-NDI$^{\bullet}$. However, no effect on the accessible capacity was seen by this operation, Figure S16. It is thus concluded that the capacity loss is irreversible and needs to be prevented rather than amended.

2.1.3. RFB-2: 50 mM 2H-NDI/BTMAP-Fc in 1 M NH_4Cl and 0.5 M NH_4Phos

In response to the effect of potassium trapping which was reported for the glycine-NDI-based battery,[40] a battery similar to RFB-1, but with ammonium instead of potassium, was assembled. Using the ammonium ion as cation has been shown to increase the solubility of AQDS[44] and ferrocyanide[45] in water almost fourfold over alkali cations, and ammonium-based background salts have frequently been used in recent flow battery studies.[17,23,44,45]

The results from RFB-2, which was based on 50 mM 2H-NDI/BTMAP-Fc in 1 M ammonium chloride and 0.5 M ammonium phosphate (NH_4Phos) are shown in Fig. 3. When changing from potassium to ammonium, the energy efficiency decreased from 87% to 83% at 10 mA cm^{-2}, see Fig. 2e and Fig. 3e respectively. However, instead of a capacity fade, a slow capacity increase was seen, and one of the most stable AORFB chemistries to date is demonstrated. Furthermore, the coulombic efficiency increased to 99.92(2)% for RFB-2 compared to 99.72(2)% of RFB–1.

After a total of 320 cycles at room temperature, the temperature was increased to 40 °C and another 100 cycles at 30 mA cm^{-2} were recorded, see Fig. 4. As seen in Fig. 4c, the temperature increase is accompanied by a drop in capacity utilization of almost 8%, but immediately starts recovering. Both the capacity drop, and its recovery are limited to the second redox couple, see Fig. 4b. The energy efficiency also sees a gradual increase, and this may be attributed to the increasing capacity of the second redox couple which corresponds to a higher battery voltage.

Cyclic voltammograms recorded after cycling show the same amount of the electroactive material as before cycling, see Figure S1b. This indicates that the ammonium cation prevents the formation of larger aggregates that are electrochemically inactive. The reason for the large differences observed for K^+ and NH_4^+ is not fully understood but is probably related to the ability of the cations to shield the negative charges on the reduced molecules. The potassium and ammonium cations have similar size and hydration properties in water. The main differences are in the local water structure in the inner hydration shell, where the ammonium ion has a smaller number of water molecules

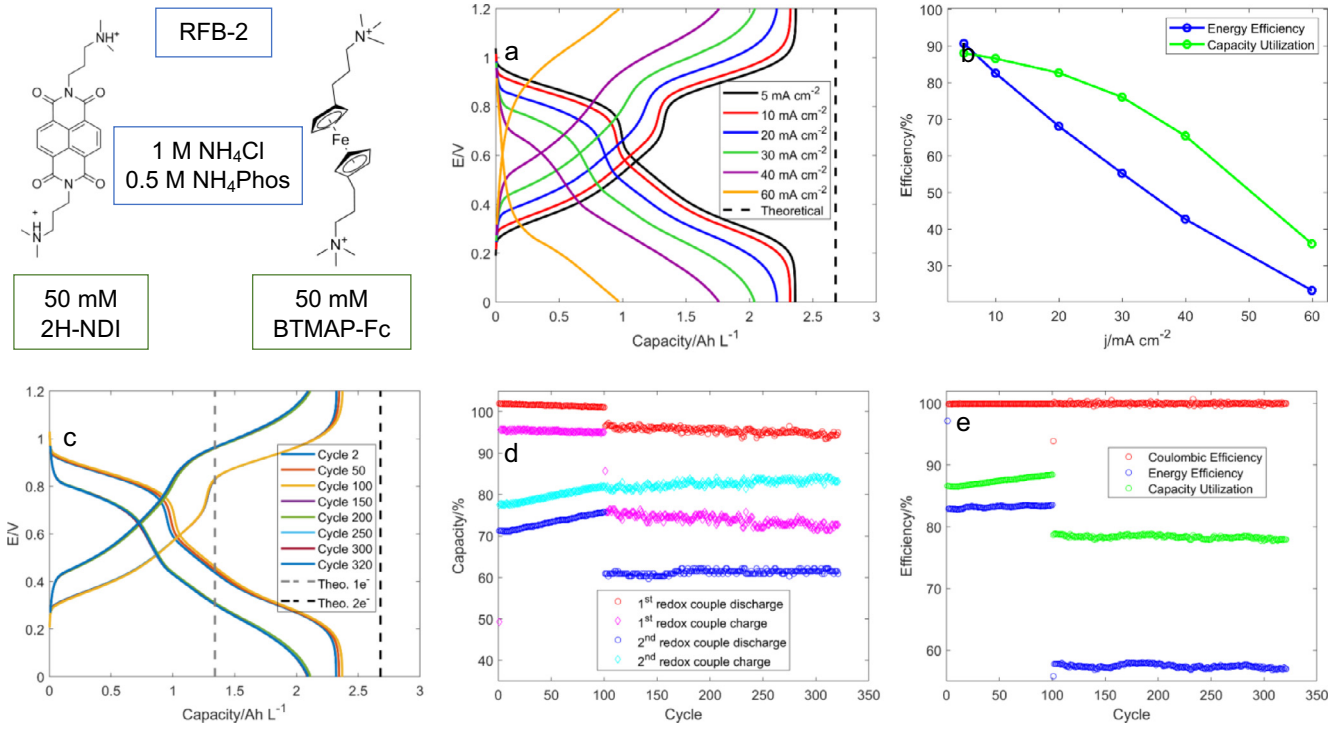

Fig. 3. Flow battery performance of 50 mM 2H-NDI and BTMAP-Fc in pH 7 0.5 M NH_4Phos and 1 M NH_4Cl solution. a) Charging and discharging curves at varying current densities, b) energy efficiency and capacity utilization at varying current densities c) charging and discharging curves at selected cycles, d) charge and discharge capacity utilization for the first and second redox couples and e) efficiencies. For the long-term cycling, a current density of 10 mA cm^{-2} was used for the first 100 cycles, and then increased to 30 mA cm^{-2} for the following 220 cycles.

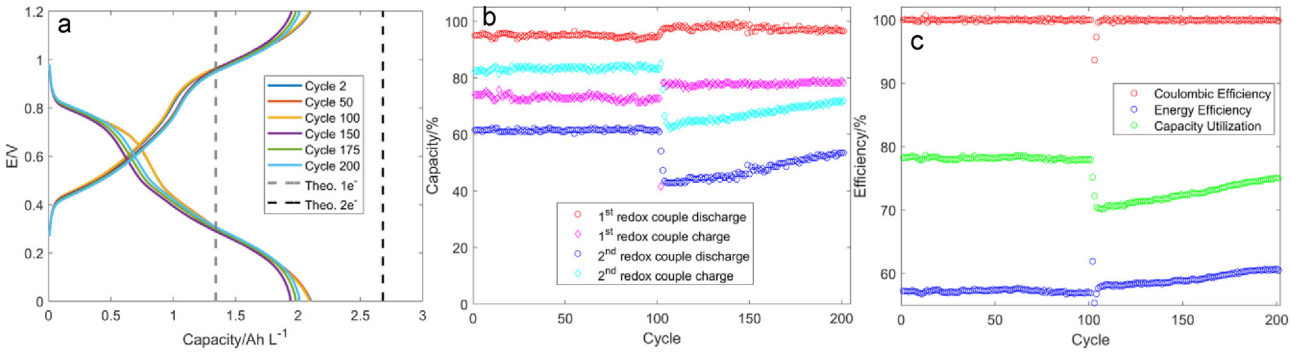

Fig. 4. RFB-2 at a temperature of 40 °C. In the above figures, the last 100 cycles at room temperature are followed by 100 cycles at 40 °C for comparison. a) Charging/discharging curves at selected cycles. Cycles 2, 50 and 100 overlap. b) Normalized capacities for the separate redox couples and c) efficiencies. Current density: 30 mA cm^{-2}.

and a more ordered water structure compared with the potassium ion [46]. For the ammonium ion there is no charge transfer from the ion to the surrounding water molecules [47].

2.1.4. RFB-3: 500 mM 2H-NDI/BTMAP-Fc in 1 M NH_4Cl and 0.5 M NH_4Phos

To study the performance of 2H-NDI at a high concentration, a redox flow battery with 500 mM 2H-NDI/BTMAP-Fc in 1 M NH_4Cl and 0.5 M NH_4Phos was assembled, see Fig. 5. At this concentration and with the dimerization constant equal to 146 [38] the dimer is dominating, i.e. 230 mM $(2H\text{-}NDI)_2$ and 40 mM 2H-NDI. Cyclic voltammograms before and after cycling are shown in Figure S2. Similar to the RFB-2 battery with 50 mM NDI, there are no differences in the peak currents before and after cycling, which clearly shows that H-NDI is stable in solution.

While the selective capacity decrease of the first electron was not seen at 50 mM active material concentration in NH_4Cl and NH_4Phos, at 500 mM the capacity fades rapidly while cycling, see Fig. 5e. Similar to the potassium-based system in RFB-1, the capacity decrease for RFB-3 was selective to the first redox couple, see Fig. 5d. It should be noted that the active material concentration in RFB-3 is ten times higher than in the other batteries but cycled with similar current densities, and the time for each cycle is thus much longer.

Even though the concentration used in RFB–3 was ten times higher than in RFB–2, the energy efficiencies at different current densities were similar between the two batteries. Furthermore, the capacity utilization in RFB–3 decreased significantly at increasing current densities, and even at a current density of 75 mA cm^{-2}, only 35% of the capacity was accessed. These effects could be explained by decreased mass transport of 2H-NDI due to its self-association. At current densities above 50 mA cm^{-2}, the first plateaus of the charging and discharging curves reach only a very small capacity before the second plateau begins, see Fig. 5a. While cycling at 25 mA cm^{-2}, the first plateau while charging was largely replaced by a long linear region due to

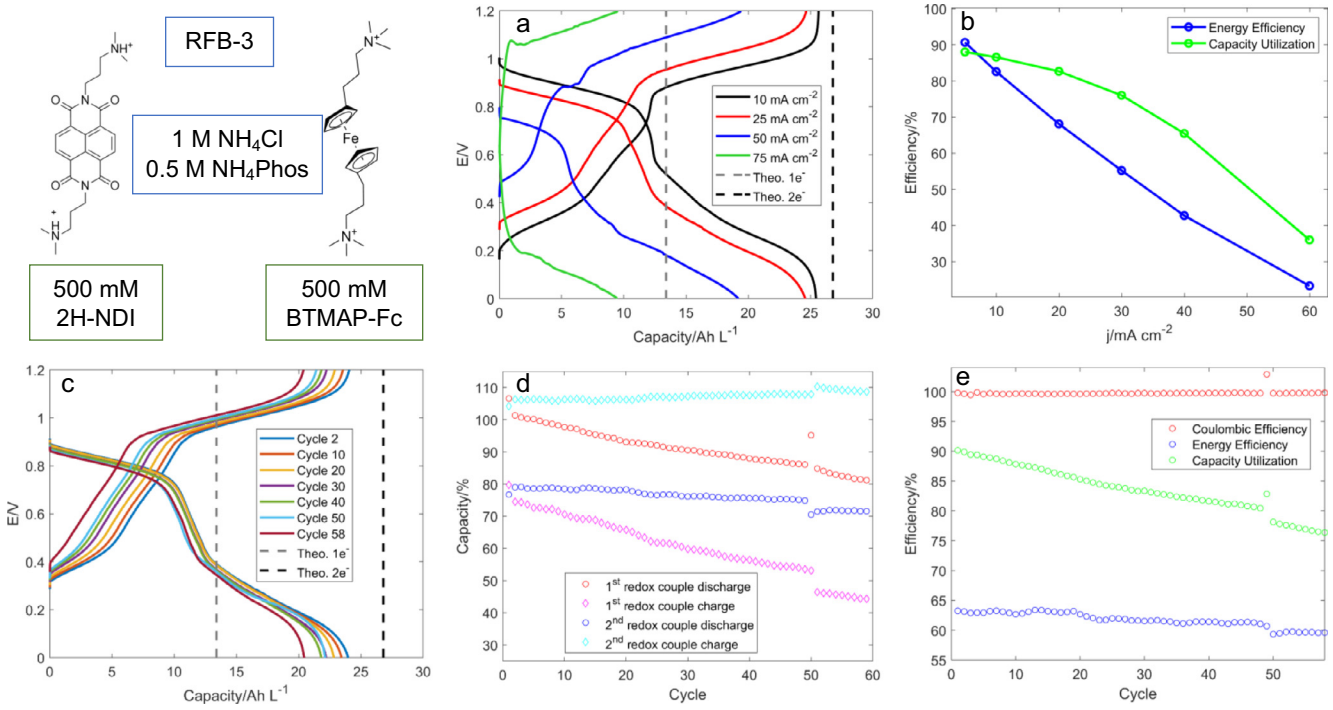

Fig. 5. Flow battery performance of 500 mM 2H-NDI/BTMAP-Fc in 1 M NH_4Cl and 0.5 M NH_4Phos. The volumes of 2H-NDI and BTMAP-Fc were 10 ml and 20 ml respectively. a) Charging and discharging curves at varying current densities, b) energy efficiency and capacity utilization at varying current densities c) charging and discharging curves at selected cycles, d) charge and discharge capacity utilization for the first and second redox couples and e) efficiencies. For the long-term cycling, a current density of 25 mA cm^{-2} was used.

the increased self-association at the high concentration, see Fig. 5c. Consequently, for the charging curves, the capacity corresponding to 0.85 V was recorded as the capacity for the first redox couple in Fig. 5d. For the discharging curves, the effect was smaller, but for consistency the capacity at 0.68 V was used.

Following the 50th charging, the battery was left at open circuit voltage for 37 h to measure the rate of self-discharge, see Fig. 6a. As seen in Fig. 6b, the discharge capacity accessed after the wait exceeded slightly that of the previous cycle, illustrating a low rate of self-discharge together with a chemical process. The capacity that was gained after the wait disappeared in the consecutive cycles, making the operation ineffective for regenerating lost capacity.

Since the amount of electrochemically active material is the same before and after cycling, the reason for the rapid decrease in capacity utilization is likely cross-over of BTMAP-Fc, see the CV in Figure S2, which mainly will influence the first redox couple.

2.2. 2DMA-NDI vs BTMAP-Fc

While 2H-NDI has two redox-couples, 2DMA-NDI only has one, and therefore only yields one voltage plateau while cycling. 2DMA-NDI, however, is reduced with two electrons coupled with two protons at neutral pH.[39] At high concentrations, this would lead to large pH-fluctuations during cycling, and could possibly be an obstacle for the application of 2DMA-NDI in applied AORFB uses.

2.2.1. RFB-4: 50 mM 2DMA-NDI/BTMAP-Fc in 1 M KCl and 0.5 M KPhos

To compare the RFB performance between 2H-NDI and 2DMA-NDI, a battery coupling 50 mM 2DMA-NDI with BTMAP-Fc in 1 M KCl and 0.5 M KPhos was assembled. In this setup, the effect of current density on capacity utilization and energy efficiency was similar to the other 50 mM batteries, see Fig. 7b.

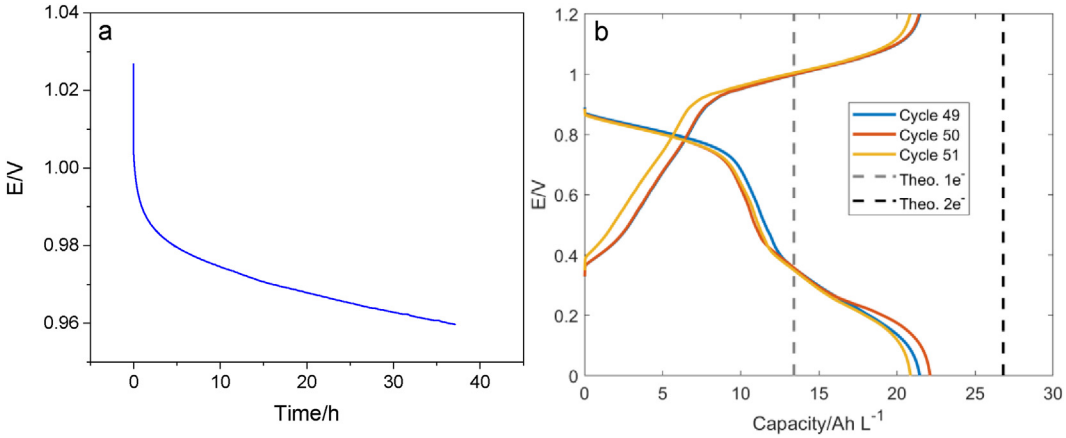

Fig. 6. Data for RFB-3, which comprised 500 mM 2H-NDI/BTMAP-Fc in 1 M NH_4Cl and 0.5 M NH_4Phos. a) Open circuit voltage (OCV) for 37 h after the 50th charge. b) Charging and discharging curves for the cycles before (cycle 49) and after (cycle 51) the OCV experiment.

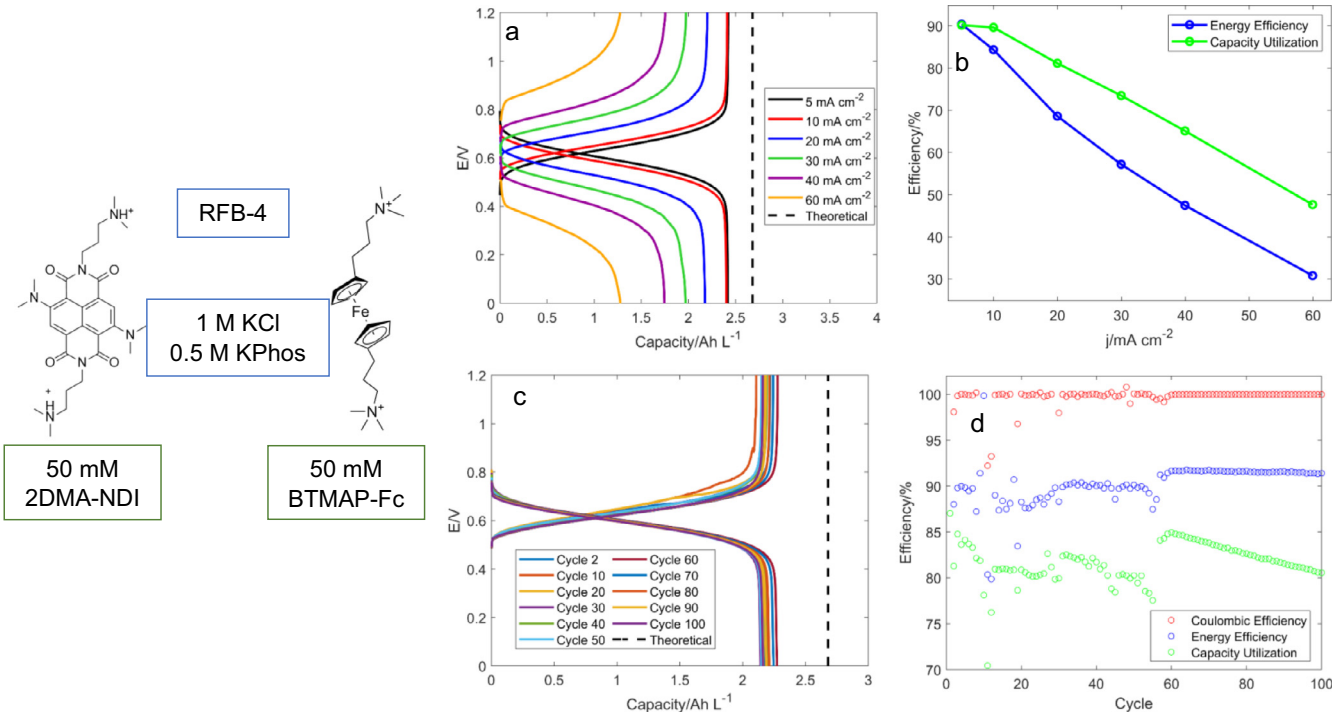

Fig. 7. Flow battery performance of 50 mM 2DMA-NDI/BTMAP-Fc in 1 M KCl and 0.5 M KPhos. a) Charging and discharging curves at varying current densities, b) energy efficiency and capacity utilization at varying current densities c) charging and discharging curves at selected cycles, d) efficiencies. For the long-term cycling, a current density of 10 mA cm^{-2} was used.

The battery was cycled at 10 mA cm^{-2} for 100 cycles, but the efficiencies fluctuated during the first 60 cycles, see Fig. 7d. This was caused by an electrolyte flow disturbance in the 2DMA-NDI reservoir, which was amended once detected, and more coherent data was acquired.

During the last 40 cycles, an average capacity fade of 0.11% per cycle at 10 mA cm^{-2} was observed, which, while significantly lower than the 0.27% seen for RFB–1, is still quite high. CVs recorded on the electrolyte reservoirs showed some crossover of BTMAP-Fc, as well as a slightly decreased peak current compared to the CVs recorded prior to RFB operation, see Figure S3. Thus, crossover of BTMAP–Fc as well as some decomposition of 2DMA–NDI in the potassium-based electrolyte were identified as the main mechanisms of capacity fade for RFB-4.

2.2.2. RFB-5: 50 mM 2DMA-NDI/BTMAP-Fc in 1 M NH_4Cl and 0.5 M NH_4Phos

An RFB with 50 mM 2DMA-NDI/BTMAP-Fc in 1 M NH_4Cl and 0.5 M NH_4Phos was assembled to see if the choice of ammonium as cation had a similar impact as for the 2H-NDI-based battery. As seen in Fig. 8b, RFB-5 performs better at higher current densities than any of the other four batteries. At 60 mA cm^{-2}, RFB-5 has an energy efficiency of 55%, compared to 30% for RFB-4, Fig. 7b. The first 100 cycles were run at a current density of 10 mA cm^{-2}, followed by 220 cycles at 30 mA cm^{-2}. Similar to RFB-2, no measurable capacity loss was seen, highlighting the high stability of the battery. Furthermore, the same gradual capacity increase was observed in the initial cycles as for RFB-2. The increasing capacity of RFB-2 indicates that the capacity of RFBs with 2DMA-NDI are also affected by self-association.

The coulombic efficiency was 99.97(2)% at 10 mA cm^{-2} and 100.00(5)% at 30 mA cm^{-2}, while the energy efficiencies were 90% and 72% for the respective current densities. The energy efficiency was seen to fluctuate and decrease slightly over the cycling time, as seen in Fig. 8d, but the magnitude of the difference is small enough to possibly be due to temperature variations or similar. Energy efficiency is known to increase with temperature as membrane, electrolyte conductivities and molecular diffusivity increase.[48]

2.3. Considerations on Self-Association and Cycling Behavior

Using ammonium instead of alkali cations as counter ion, as mentioned earlier, has been shown to significantly increase the solubility of AQDS and ferrocyanide.[44,45] In the case of AQDS, the ammonium ions were proposed to form hydrogen bonds to the carbonyl oxygen atoms,[44] and thus electrostatically shield the molecules from each other. Two main trends on cycling behavior was seen in the present article. Firstly, the capacity loss while cycling mainly affects the first redox couple, however, in the case of 2DMA-NDI, this distinction cannot be made. One explanation could be that the electrolyte containing BTMAP-Fc was either parasitically reduced back from its oxidized state by another process or decomposed in its oxidized state by oxygen.[49] Either way, the process for 2H-$NDI^{\bullet}$ to be oxidized back to 2H-NDI would be limited.

Another explanation was sought using DFT calculations on the redox behavior of the 2H-NDI dimer. Potentials and equilibrium constants of dimerization were acquired for a number of relevant structures, see Section 8 in the SI. It was generally seen that the equilibrium constants favored self-association, with values ranging between K = 792 in the case of the oxidized species, $(2H\text{-}NDI)_2$, and K = $1.8{\cdot}10^{10}$ between 2H-NDI and $2H\text{-}NDI^{2-}$ forming $(2H\text{-}NDI)_2^{2-}$. However, the two latter species hardly occur simultaneously during electrolysis, and a more likely scenario is the association between 2H-NDI and $2H\text{-}NDI^{\bullet}$ to form $(2H\text{-}NDI)_2^{\bullet}$, for which K = $1.7{\cdot}10^{4}$. The dimer $(2H\text{-}NDI)_2$ can be reduced with two electrons in the first redox couple, i.e. one electron per monomer, also forming the dianion of the dimer, $(2H\text{-}NDI)_2^{2-}$. The third and fourth electron transfer to the dimer occur at more negative potentials in the range of the second redox couple, see the simulated CV in Figure S17. In contrast to the experimental data, a separate peak is observed for the fourth electron

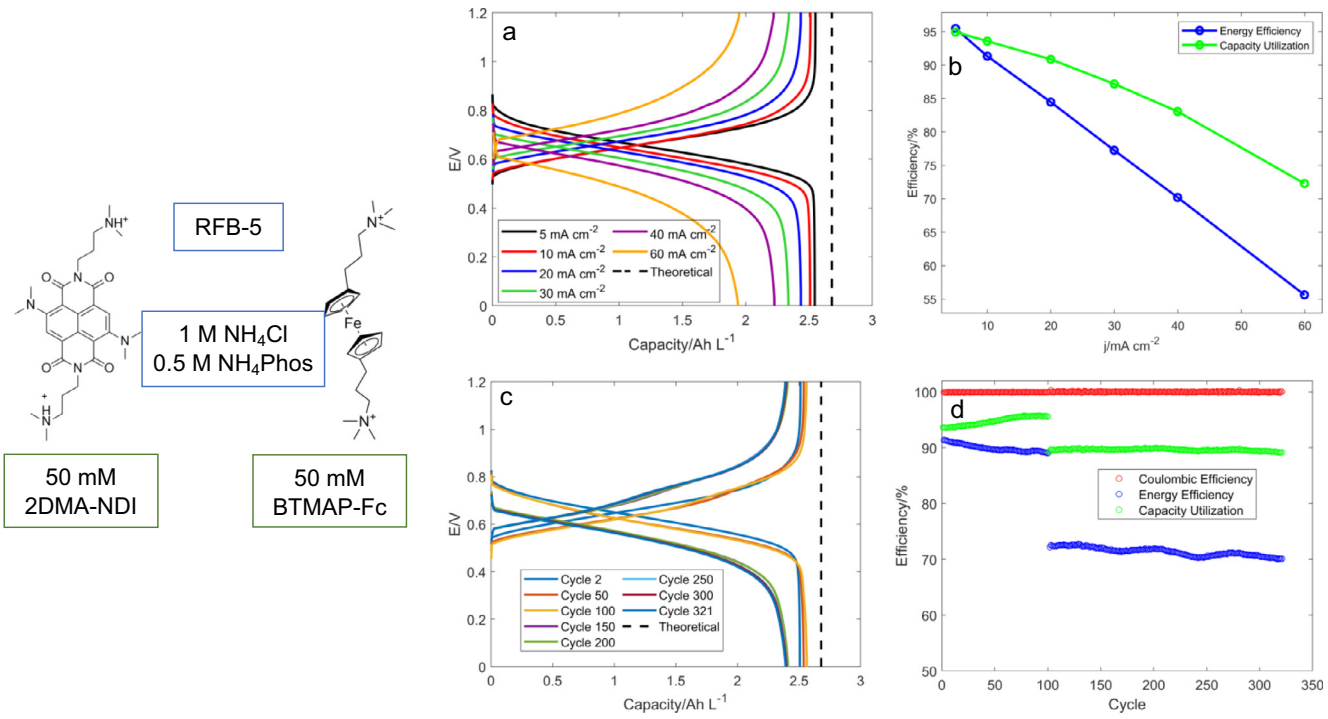

Fig. 8. Flow battery performance of 50 mM 2DMA-NDI/BTMAP-Fc in 1 M NH_4Cl and 0.5 M NH_4Phos. a) charging and discharging curves at varying current densities, b) energy efficiency and capacity utilization at varying current densities c) charging and discharging curves at selected cycles, d) efficiencies. For the long-term cycling, a current density of 10 mA cm^{-2} was used for the first 100 cycles, and then increased to 30 mA cm^{-2} for the following 220 cycles.

transfer. One possible explanation is that the interaction with electrolyte cations will lower the charge of the molecule and move the potential for the most negative complexes in positive direction. It should be noted that in the DFT calculations the charged side chains of the 2H-NDI molecule are truncated and therefore some electrostatic repulsion and steric hindrance between molecules are not considered. This probably explains the difference in equilibrium constant for the formation of $(2H\text{-}NDI)_2$ obtained experimentally and by DFT calculations, 146 [38] and 792 [39] respectively. It can be concluded that dimer formation at different stages in the reduction process is not enough to explain the capacity loss in the batteries.

Furthermore, it was hypothesized that any self-associative capacity loss could be reversed by applying potentiostatic holds. In this scenario, as the first redox couple consistently suffered the largest capacity loss, it seemed probable that the capacity-reducing self-associative species involves $2H\text{-}NDI^{-\bullet}$. Therefore, it was thought that the equilibrium of this self-association should be possible to drive toward either $2H\text{-}NDI^{2-}$ or 2H-NDI by applying potentiostatic holds at either a high or low enough voltage respectively. However, as shown in SI sections 4, 6 and 7, such treatments were ineffective.

It is concluded that the capacity decrease is related to a loss of active material during cycling, possibly related to formation of larger aggregates, and to some cross-over of BTMAP-Fc.

3. Conclusion

2H-NDI and 2DMA-NDI were clearly demonstrated as highly promising candidates for pH-neutral aqueous organic redox flow batteries, but measures for reducing self-association are needed.

Three redox flow batteries coupling 2H-NDI with BTMAP-Fc were demonstrated with varying levels of performance. 2H-NDI at 50 mM in 1 M KCl and 0.5 M KPhos showed high energy efficiency and capacity utilization but had a capacity loss of 31% over 197 cycles, with most of the capacity loss stemming from the first redox couple. Replacing the potassium cation in the supporting electrolyte with ammonium, a remarkable cycling stability was obtained over 320 cycles, showing one of the most stable chemistries to date. However, upon increasing the concentration of the active materials to 500 mM, significant capacity loss was observed mainly due to cross-over of BTMAP-Fc.

The best performance was observed for the core-substituted dimethylamino-NDI (2DMA-NDI). Two redox flow batteries with 50 mM 2DMA-NDI coupled with were studied, one with 1 M KCl and 0.5 M KPhos as supporting electrolyte, and the other with the ammonium equivalent. Similar to 2H–NDI, an astonishing increase in cycling stability was demonstrated for 2DMA-NDI when changing from potassium to ammonium as cation, and only a capacity increase was seen over the first 100 cycles before levelling out at a constant value for the following 220 cycles.

In order to optimize the performance of AORFBs with NDI substances, tests with higher concentrations and extended cycling are necessary to give better information on the long-term stability of the systems. For future development, the NDI molecules need to be core-substituted to limit self-association and the choice of electrolyte cation needs to be considered as well as the end groups that enable high solubility in aqueous solution.

4. Experimental and computational details

The investigated NDI materials were synthesized according to previously reported procedures.[38,39] BTMAP-Fc (98%) was purchased from TCI.

A Gamry Reference 600 potentiostat was used for all electrochemical analyses. **Cyclic Voltammetry:** A 3 mm diameter glassy carbon working electrode (BASi) was polished with alumina (0.3 μm, Struers AP-D), rinsed with deionized water and then sonicated for at least one minute in deionized water. As counter electrode, a platinum mesh was used and as reference electrode, Ag/AgCl in 3 M NaCl (BASi), E = 0.214 V vs NHE. Voltammograms at scan rates of 20, 50 and 100, 250 and 500 mV s^{-1} were collected. **Flow Battery Operation:** A 5 cm^2 flow battery (Scribner) was used, with an interdigitated graphite flow field and SGL Carbon SIGRACELL electrodes without pretreatment. A Selemion DSV membrane which had been stored in 0.25 M NaCl was used after having been washed and left in the to-be-used electrolyte for at least a day. A peristaltic pump (Lead Flow BT600L) with Masterflex C-Flex tubing (Cole-Parmer) was used with a flow rate of 60 ml min^{-1}. The entire flow battery setup was encapsulated in a glovebag (AtmosBag, Sigma Aldrich) which was purged and pressurized with nitrogen gas. The electrolyte volumes were 10 ml for the negative electrolyte (2H-NDI or 2DMA-NDI) and 20 ml for the positive electrolyte (BTMAP-Fc). After assembling a battery with a certain electrolyte, an impedance spectrum was recorded to acquire the internal resistance of the cell. This was followed by three galvanostatic charging/discharging cycles at varying current densities, from which the third cycle was used for analysis on current density dependencies. Finally, a larger number of galvanostatic charging/discharging cycles were carried out at set current density. The capacity utilization was calculated by dividing the accessed discharge capacity by the theoretical capacity. The energy efficiency was calculated by numerically integrating the plots of capacity versus voltage for the discharging curve. and dividing it by the same for the charge curve. The integration was carried out using MATLAB's trapz function. **Electrochemical Impedance Spectroscopy:** Potentiostatic EIS spectra were recorded at a frequency range between 100 kHz and 100 mHz, with a 10 mV RMS potential perturbation from open circuit voltage and 9 points per decade. **pH Measurements** were performed using a Metrohm 827 pH lab pH-meter calibrated using buffer solutions (VWR) with pH = 12.00, 9.00 and 4.00.

DFT calculations were performed using Gaussian 16 Rev. B.01 [50] in combination with the M06–2X functional and a triple-ζ $6\text{–}311++G^{**}$ basis set with diffuse and polarization functions on all atoms.[51] Solvation was treated using the implicit SMD solvation model as implemented into Gaussian 16.[52] Convergence of the structures to the minimum was ensured by testing for, and removal of, all imaginary frequencies. For further details see reference.[53]

Declaration of Competing Interest

The authors declare that they have no known competing financial interests or personal relationships that could have appeared to influence the work reported in this paper.

Acknowledgements

This work was supported by the Swedish Research Council (grant 2015-04853) and the Swedish Research Council FORMAS (grant 942-2015-411).

Appendix A. Supplementary data

Supplementary data to this article can be found online at https://doi.org/10.1016/j.jelechem.2021.115224.

References

[1] A. Narayanan, K. Mets, M. Strobbe, C. Develder, Feasibility of 100% renewable energy-based electricity production for cities with storage and flexibility, Renewable Energy 134 (2019) 698–709, https://doi.org/10.1016/j.renene.2018.11.049.

[2] W. Liu, W. Lu, H. Zhang, X. Li, Aqueous Flow Batteries: Research and Development, Chemistry – A, European Journal 25 (7) (2019) 1649–1664, https://doi.org/10.1002/chem.v25.710.1002/chem.201802798.

[3] B. Dunn, H. Kamath, J.M. Tarascon, Electrical energy storage for the grid: a battery of choices, Science 334 (6058) (2011) 928–935, https://doi.org/10.1126/science.1212741.

[4] P. Leung, X. Li, C. Ponce de León, L. Berlouis, C.T.J. Low, F.C. Walsh, Progress in redox flow batteries, remaining challenges and their applications in energy storage, RSC Adv. 2 (27) (2012) 10125–10156, https://doi.org/10.1039/C2RA21342G.

[5] W. Wang, Q. Luo, B. Li, X. Wei, L. Li, Z. Yang, Recent Progress in Redox Flow Battery Research and Development, Adv. Funct. Mater. 23 (8) (2013) 970–986, https://doi.org/10.1002/adfm.v23.810.1002/adfm.201200694.

[6] F. Pan, Q. Wang, Redox Species of Redox Flow Batteries: A Review, Molecules 20 (11) (2015) 20499–20517, https://doi.org/10.3390/molecules201119711.

[7] J. Winsberg, T. Hagemann, T. Janoschka, M.D. Hager, U.S. Schubert, Redox-Flow Batteries: From Metals to Organic Redox-Active Materials, Angew. Chem. Int. Ed. Engl. 56 (3) (2017) 686–711, https://doi.org/10.1002/anie.v56.310.1002/anie.201604925.

[8] M.A. Escalante Soberanis, T. Mithrush, A. Bassam, W. Mérida, A sensitivity analysis to determine technical and economic feasibility of energy storage systems implementation: A flow battery case study, Renewable Energy 115 115 (2018) 547–557, https://doi.org/10.1016/j.renene.2017.08.082.

[9] B. Huskinson, M.P. Marshak, C. Suh, S. Er, M.R. Gerhardt, C.J. Galvin, X. Chen, A. Aspuru-Guzik, R.G. Gordon, M.J. Aziz, A metal-free organic-inorganic aqueous flow battery, Nature 505 (7482) (2014) 195–198, https://doi.org/10.1038/nature12909.

[10] M. Park, E.S. Beh, E.M. Fell, Y. Jing, E.F. Kerr, D. Porcellinis, M.-A. Goulet, J. Ryu, A.A. Wong, R.G. Gordon, J. Cho, M.J. Aziz, A High Voltage Aqueous Zinc-Organic Hybrid Flow Battery, Adv. Energy Mater. 9 (25) (2019) 1900694, https://doi.org/10.1002/aenm.v9.2510.1002/aenm.201900694.

[11] D.P. Tabor, R. Gómez-Bombarelli, L. Tong, R.G. Gordon, M.J. Aziz, A. Aspuru-Guzik, Mapping the frontiers of quinone stability in aqueous media: implications for organic aqueous redox flow batteries, J. Mater. Chem. A 7 (20) (2019) 12833–12841, https://doi.org/10.1039/c9ta03219c.

[12] Y. Liu, M.-A. Goulet, L. Tong, Y. Liu, Y. Ji, L. Wu, R.G. Gordon, M.J. Aziz, Z. Yang, T. Xu, A Long-Lifetime All-Organic Aqueous Flow Battery Utilizing TMAP-TEMPO Radical, Chem 5 (7) (2019) 1861–1870, https://doi.org/10.1016/j.chempr.2019.04.021.

[13] J. Luo, B. Hu, C. Debruler, T.L. Liu, A pi-Conjugation Extended Viologen as a Two-Electron Storage Anolyte for Total Organic Aqueous Redox Flow Batteries, Angew. Chem. Int. Ed. Engl. 57 (1) (2018) 231–235, https://doi.org/10.1002/anie.201710517.

[14] T. Hagemann, J. Winsberg, M. Grube, I. Nischang, T. Janoschka, N. Martin, M.D. Hager, U.S. Schubert, An aqueous all-organic redox-flow battery employing a (2,2,6,6-tetramethylpiperidin-1-yl)oxyl-containing polymer as catholyte and dimethyl viologen dichloride as anolyte, J. Power Sources 378 (2018) 546–554, https://doi.org/10.1016/j.jpowsour.2017.09.007.

[15] T. Janoschka, C. Friebe, M.D. Hager, N. Martin, U.S. Schubert, An Approach Toward Replacing Vanadium: A Single Organic Molecule for the Anode and Cathode of an Aqueous Redox-Flow Battery, ChemistryOpen 6 (2) (2017) 216–220, https://doi.org/10.1002/open.v6.210.1002/open.201600155.

[16] E.S. Beh, D. De Porcellinis, R.L. Gracia, K.T. Xia, R.G. Gordon, M.J. Aziz, A Neutral pH Aqueous Organic-Organometallic Redox Flow Battery with Extremely High Capacity Retention, ACS Energy Lett. 2 (3) (2017) 639–644, https://doi.org/10.1021/acsenergylett.7b0001910.1021/acsenergylett.7b00019.s001.

[17] A. Khataee, K. Wedege, E. Dražević, A. Bentien, Differential pH as a method for increasing cell potential in organic aqueous flow batteries, J. Mater. Chem. A 5 (41) (2017) 21875–21882, https://doi.org/10.1039/c7ta04975g.

[18] A. Orita, M.G. Verde, M. Sakai, Y.S. Meng, A biomimetic redox flow battery based on flavin mononucleotide, Nat Commun 7 (2016) 13230, https://doi.org/10.1038/ncomms13230.

[19] Y. Ji, M.-A. Goulet, D.A. Pollack, D.G. Kwabi, S. Jin, D. Porcellinis, E.F. Kerr, R.G. Gordon, M.J. Aziz, A Phosphonate-Functionalized Quinone Redox Flow Battery at Near-Neutral pH with Record Capacity Retention Rate, Adv. Energy Mater. 9 (12) (2019) 1900039, https://doi.org/10.1002/aenm.v9.1210.1002/aenm.201900039.

[20] C. Wiberg, T.J. Carney, F. Brushett, E. Ahlberg, E. Wang, Dimerization of 9,10-anthraquinone-2,7-Disulfonic acid (AQDS), Electrochim. Acta 317 (2019) 478–485, https://doi.org/10.1016/j.electacta.2019.05.134.

[21] S. Jin, Y. Jing, D.G. Kwabi, Y. Ji, L. Tong, D. De Porcellinis, M.-A. Goulet, D.A. Pollack, R.G. Gordon, M.J. Aziz, A Water-Miscible Quinone Flow Battery with High Volumetric Capacity and Energy Density, ACS Energy Lett. 4 (6) (2019) 1342–1348, https://doi.org/10.1021/acsenergylett.9b0073910.1021/acsenergylett.9b00739.s001.

[22] D.G. Kwabi, K. Lin, Y. Ji, E.F. Kerr, M.-A. Goulet, D. De Porcellinis, D.P. Tabor, D.A. Pollack, A. Aspuru-Guzik, R.G. Gordon, M.J. Aziz, Alkaline Quinone Flow Battery with Long Lifetime at pH 12, Joule 2 (9) (2018) 1894–1906, https://doi.org/10.1016/j.joule.2018.07.005.

[23] A. Khataee, E. Dražević, J. Catalano, A. Bentien, Performance Optimization of Differential pH Quinone-Bromide Redox Flow Battery, J. Electrochem. Soc. 165 (16) (2018) A3918–A3924, https://doi.org/10.1149/2.0681816jes.

[24] T. Janoschka, N. Martin, U. Martin, C. Friebe, S. Morgenstern, H. Hiller, M.D. Hager, U.S. Schubert, An aqueous, polymer-based redox-flow battery using non-corrosive, safe, and low-cost materials, Nature 527 (7576) (2015) 78–81, https://doi.org/10.1038/nature15746.

[25] W. Liu, Y. Liu, H. Zhang, C. Xie, L. Shi, Y.-G. Zhou, X. Li, A highly stable neutral viologen/bromine aqueous flow battery with high energy and power density, Chem. Commun. 55 (33) (2019) 4801–4804, https://doi.org/10.1039/C9CC00840C.

[26] S.V. Bhosale, C.H. Jani, S.J. Langford, Chemistry of naphthalene diimides, Chem. Soc. Rev. 37 (2) (2008) 331–342, https://doi.org/10.1039/B615857A.

[27] N. Zhou, A. Facchetti, Naphthalenediimide (NDI) polymers for all-polymer photovoltaics, Mater. Today 21 (4) (2018) 377–390, https://doi.org/10.1016/j.mattod.2018.02.003.

[28] J.M. Bjuggren, A. Sharma, D. Gedefaw, S. Elmas, C. Pan, B. Kirk, X. Zhao, G. Andersson, M.R. Andersson, Facile Synthesis of an Efficient and Robust Cathode Interface Material for Polymer Solar Cells, ACS Applied Energy Materials 1 (12) (2018) 7130–7139, https://doi.org/10.1021/acsaem.8b0155410.1021/acsaem.8b01554.s001.

[29] L. Zong, Y. Xie, C. Wang, J.-R. Li, Q. Li, Z. Li, From ACQ to AIE: the suppression of the strong π–π interaction of naphthalene diimide derivatives through the adjustment of their flexible chains, Chem. Commun. 52 (77) (2016) 11496–11499, https://doi.org/10.1039/C6CC06176A.

[30] P. Rajdev, M.R. Molla, S. Ghosh, Understanding the Role of H-Bonding in Aqueous Self-Assembly of Two Naphthalene Diimide (NDI)-Conjugated Amphiphiles, Langmuir 30 (8) (2014) 1969–1976, https://doi.org/10.1021/la500089b.

[31] F. Doria, M. Nadai, G. Sattin, L. Pasotti, S.N. Richter, M. Freccero, Water soluble extended naphthalene diimides as pH fluorescent sensors and G-quadruplex ligands, Org Biomol Chem 10 (19) (2012) 3830–3840, https://doi.org/10.1039/c2ob07006e.

[32] A.R. Smith B. Iverson 37 71 10.1039/9781782621386-00037

[33] A. Weißenstein, V. Grande, C.R. Saha-Möller, F. Würthner, Water-soluble naphthalene diimides: synthesis, optical properties, and colorimetric detection of biogenic amines, Org. Chem. Front. 5 (18) (2018) 2641–2651, https://doi.org/10.1039/c8qo00611c.

[34] Q. Lin, L. Liu, F. Zheng, P.-P. Mao, J. Liu, Y.-M. Zhang, H. Yao, T.-B. Wei, A benzimidazole functionalized NDI derivative for recyclable fluorescent detection of cyanide in water, RSC Adv. 7 (61) (2017) 38458–38462, https://doi.org/10.1039/C7RA07247C.

[35] Y. Shi, H. Tang, S. Jiang, L.V. Kayser, M. Li, F. Liu, F. Ji, D.J. Lipomi, S.P. Ong, Z. Chen, Understanding the Electrochemical Properties of Naphthalene Diimide: Implication for Stable and High-Rate Lithium-Ion Battery Electrodes, Chem. Mater. 30 (10) (2018) 3508–3517, https://doi.org/10.1021/acs.chemmater.8b0130410.1021/acs.chemmater.8b01304.s001.

[36] G.S. Vadehra, R.P. Maloney, M.A. Garcia-Garibay, B. Dunn, Naphthalene Diimide Based Materials with Adjustable Redox Potentials: Evaluation for Organic Lithium-Ion Batteries, Chem. Mater. 26 (24) (2014) 7151–7157, https://doi.org/10.1021/cm503800r.

[37] D.J. Kim, S.H. Je, S. Sampath, J.W. Choi, A. Coskun, Effect of N-substitution in naphthalenediimides on the electrochemical performance of organic rechargeable batteries, RSC, Advances 2 (21) (2012) 7968, https://doi.org/10.1039/c2ra21239k.

[38] C. Wiberg, F. Owusu, E. Wang, E. Ahlberg, Electrochemical Evaluation of a Napthalene Diimide Derivative for Potential Application in Aqueous Organic Redox Flow Batteries, Energy Technology 7 (11) (2019) 1900843, https://doi.org/10.1002/ente.v7.1110.1002/ente.201900843.

[39] C. Wiberg, M. Busch, L. Evenäs, E. Ahlberg, The Electrochemical Response of Core-Functionalized Naphthalene Diimides (NDI) – A Combined Computational and Experimental Investigation, Electrochim. Acta 367 (2021) 137480, https://doi.org/10.1016/j.electacta.2020.137480.

[40] V. Medabalmi, M. Sundararajan, V. Singh, M.-H. Baik, H.R. Byon, Naphthalene diimide as a two-electron anolyte for aqueous and neutral pH redox flow batteries, J. Mater. Chem. A 8 (22) (2020) 11218–11223, https://doi.org/10.1039/d0ta01160f.

[41] M. Zhou, Y. Chen, M. Salla, H. Zhang, X. Wang, S.R. Mothe, Q. Wang, Single-Molecule Redox-Targeting Reactions for a pH-Neutral Aqueous Organic Redox Flow Battery, Angew. Chem. Int. Ed. Engl. 59 (34) (2020) 14286–14291, https://doi.org/10.1002/anie.v59.3410.1002/anie.202004603.

[42] J. Luo, W. Wu, C. Debruler, B. Hu, M. Hu, T.L. Liu, A, 1.51 v pH neutral redox flow battery towards scalable energy storage, J. Mater. Chem. A 7 (15) (2019) 9130–9136, https://doi.org/10.1039/c9ta01469a.

[43] Bo Hu, Camden DeBruler, Zayn Rhodes, T. Leo Liu, Long-Cycling Aqueous Organic Redox Flow Battery (AORFB) toward Sustainable and Safe Energy Storage, J. Am. Chem. Soc. 139 (3) (2017) 1207–1214, https://doi.org/10.1021/jacs.6b1098410.1021/jacs.6b10984.s001.

[44] Bo Hu, Jian Luo, Maowei Hu, Bing Yuan, T. Leo Liu, A pH-Neutral, Metal-Free Aqueous Organic Redox Flow Battery Employing an Ammonium Anthraquinone Anolyte, Angew. Chem. Int. Ed. Engl. 58 (46) (2019) 16629–16636, https://doi.org/10.1002/anie.v58.4610.1002/anie.201907934.

[45] J. Luo, B. Hu, C. Debruler, Y. Bi, Y. Zhao, B. Yuan, M. Hu, W. Wu, T.L. Liu, Unprecedented Capacity and Stability of Ammonium Ferrocyanide Catholyte in pH Neutral Aqueous Redox Flow Batteries, Joule 3 (1) (2019) 149–163, https://doi.org/10.1016/j.joule.2018.10.010.

[46] F. Aydin, C. Zhan, C. Ritt, R. Epsztein, M. Elimelech, E. Schwegler, T.A. Pham, Similarities and differences between potassium and ammonium ions in liquid water: a first-principles study, PCCP 22 (4) (2020) 2540–2548, https://doi.org/10.1039/c9cp06163k.

[47] Maria Ekimova, Wilson Quevedo, Łukasz Szyc, Marcella Iannuzzi, Philippe Wernet, Michael Odelius, Erik T.J. Nibbering, Aqueous Solvation of Ammonia and Ammonium: Probing Hydrogen Bond Motifs with FT-IR and Soft X-ray Spectroscopy, J. Am. Chem. Soc. 139 (36) (2017) 12773–12783, https://doi.org/10.1021/jacs.7b0720710.1021/jacs.7b07207.s001.

[48] Q. Chen, M.R. Gerhardt, L. Hartle, M.J. Aziz, A Quinone-Bromide Flow Battery with 1 W/cm2 Power Density, J. Electrochem. Soc. 163 (1) (2015) A5010–A5013, https://doi.org/10.1149/2.0021601jes.

[49] J.P. Hurvois, C. Moinet, Reactivity of ferrocenium cations with molecular oxygen in polar organic solvents: Decomposition, redox reactions and stabilization, J. Organomet. Chem. 690 (7) (2005) 1829–1839, https://doi.org/10.1016/j.jorganchem.2005.02.009.

[50] M.J. Frisch, G.W. Trucks, H.B. Schlegel, G.E. Scuseria, M.A. Robb, J.R. Cheeseman, G. Scalmani, V. Barone, G.A. Petersson, H. Nakatsuji, X. Li, M. Caricato, A.V. Marenich, J. Bloino, B.G. Janesko, R. Gomperts, B. Mennucci, H.P. Hratchian, J.V. Ortiz, A.F. Izmaylov, J.L. Sonnenberg, Williams, F. Ding, F. Lipparini, F. Egidi, J. Goings, B. Peng, A. Petrone, T. Henderson, D. Ranasinghe, V.G. Zakrzewski, J. Gao, N. Rega, G. Zheng, W. Liang, M. Hada, M. Ehara, K. Toyota, R. Fukuda, J. Hasegawa, M. Ishida, T. Nakajima, Y. Honda, O. Kitao, H. Nakai, T. Vreven, K. Throssell, J.A. Montgomery Jr., J.E. Peralta, F. Ogliaro, M.J. Bearpark, J.J. Heyd, E.N. Brothers, K.N. Kudin, V.N. Staroverov, T.A. Keith, R. Kobayashi, J. Normand, K. Raghavachari, A.P. Rendell, J.C. Burant, S.S. Iyengar, J. Tomasi, M. Cossi, J.M. Millam, M. Klene, C. Adamo, R. Cammi, J.W. Ochterski, R.L. Martin, K. Morokuma, O. Farkas, J.B. Foresman, D.J. Fox, Gaussian 16 Rev. C.01, Wallingford, CT, 2016.

[51] Y. Zhao, D.G. Truhlar, The M06 suite of density functionals for main group thermochemistry, thermochemical kinetics, noncovalent interactions, excited states, and transition elements: two new functionals and systematic testing of four M06-class functionals and 12 other functionals, Theor. Chem. Acc. 120 (1) (2008) 215–241, https://doi.org/10.1007/s00214-007-0310-x.

[52] A.V. Marenich, C.J. Cramer, D.G. Truhlar, Universal solvation model based on solute electron density and on a continuum model of the solvent defined by the bulk dielectric constant and atomic surface tensions, J. Phys. Chem. B 113 (18) (2009) 6378–6396, https://doi.org/10.1021/jp810292n.

[53] M. Busch, K. Laasonen, E. Ahlberg, Method for the accurate prediction of electron transfer potentials using an effective absolute potential, Phys. Chem. Chem. Phys. 22 (44) (2020) 25833–25840, https://doi.org/10.1039/d0cp04508j.